

# Collective oscillations of a stored deuteron beam close to the quantum limit

J. Slim<sup>1</sup>, N.N. Nikolaev<sup>2</sup>, F. Rathmann<sup>3</sup>, A. Wirzba<sup>3,4</sup>, A. Nass<sup>3</sup>, V. Hejny<sup>3</sup>, J. Pretz<sup>3</sup>, H. Soltner<sup>5</sup>, F. Abusaif<sup>3</sup>, A. Aggarwal<sup>6</sup>, A. Aksentev<sup>7</sup>, A. Andres<sup>1</sup>, L. Barion<sup>8</sup>, G. Ciullo<sup>8</sup>, S. Dymov<sup>8,9</sup>, R. Gebel<sup>3</sup>, M. Gaisser<sup>1</sup>, K. Grigoryev<sup>3</sup>, D. Grzonka<sup>3</sup>, O. Javakhishvili<sup>10</sup>, A. Kacharava<sup>3</sup>, V. Kamerdzhev<sup>3</sup>, S. Karanth<sup>6</sup>, I. Keshelashvili<sup>3</sup>, P. Lenisa<sup>8</sup>, N. Lomidze<sup>11</sup>, B. Lorentz<sup>12</sup>, A. Magiera<sup>6</sup>, D. Mchedlishvili<sup>11</sup>, F. Müller<sup>1</sup>, A. Pesce<sup>3</sup>, V. Poncza<sup>3</sup>, D. Prasuhn<sup>3</sup>, A. Saleev<sup>8</sup>, V. Shmakova<sup>3,9</sup>, H. Ströher<sup>3</sup>, M. Tabidze<sup>11</sup>, G. Tagliente<sup>13</sup>, Y. Valdau<sup>3</sup>, T. Wagner<sup>3</sup>, C. Weidemann<sup>3</sup>, A. Wrońska<sup>6</sup>, and M. Żurek<sup>14</sup>

<sup>1</sup>*III. Physikalisches Institut B, RWTH Aachen University, 52056 Aachen, Germany*

<sup>2</sup>*L.D. Landau Institute for Theoretical Physics, 142432 Chernogolovka, Russia*

<sup>3</sup>*Institut für Kernphysik, Forschungszentrum Jülich, 52425 Jülich, Germany*

<sup>4</sup>*Institute for Advanced Simulation, Forschungszentrum Jülich, 52425 Jülich, Germany*

<sup>5</sup>*Zentralinstitut für Engineering, Elektronik und Analytik, Forschungszentrum Jülich, 52425 Jülich, Germany*

<sup>6</sup>*Marian Smoluchowski Institute of Physics, Jagiellonian University, 30348 Cracow, Poland*

<sup>7</sup>*Institute for Nuclear Research, Russian Academy of Sciences, 117312 Moscow, Russia*

<sup>8</sup>*University of Ferrara and Istituto Nazionale di Fisica Nucleare, 44100 Ferrara, Italy*

<sup>9</sup>*Laboratory of Nuclear Problems, Joint Institute for Nuclear Research, 141980 Dubna, Russia*

<sup>10</sup>*Department of Electrical and Computer Engineering, Agricultural University of Georgia, 0159 Tbilisi, Georgia*

<sup>11</sup>*High Energy Physics Institute, Tbilisi State University, 0186 Tbilisi, Georgia*

<sup>12</sup>*GSI Helmholtzzentrum für Schwerionenforschung, 64291 Darmstadt, Germany*

<sup>13</sup>*Istituto Nazionale di Fisica Nucleare sez. Bari, 70125 Bari, Italy*

<sup>14</sup>*Lawrence Berkeley National Laboratory, Berkeley, California 94720, USA*

December 23, 2024

We investigated coherent betatron oscillations of a deuteron beam in the storage ring COSY, excited by a detuned radio-frequency Wien filter. These beam oscillations were detected by conventional beam position monitors, read out with lock-in amplifiers. The response of the stored beam to the detuned Wien filter was modelled using the ring lattice and time-dependent 3D field maps of the radio-frequency Wien filter. The influence of uncertain system parameters related to manufacturing tolerances and electronics was investigated using the

**polynomial chaos expansion. With the currently available apparatus, we show that oscillation amplitudes down to  $1\text{ }\mu\text{m}$  can be detected. Future measurements of the electric dipole moment of protons will, however, require control of the relative position of counter-propagating beams in the sub-picometer range. Since the stored beam can be considered as a rarefied gas of uncorrelated particles, we moreover demonstrate that the amplitudes of the zero-point betatron oscillations of individual particles are within a factor of 10 of the Heisenberg uncertainty limit. As a consequence of this, we conclude that quantum mechanics does not preclude the control of the beam centroids to sub-picometer accuracy. The smallest Lorentz force exerted on a single particle that we have been able to determine is  $10\text{ aN}$ .**

## 1 Introduction

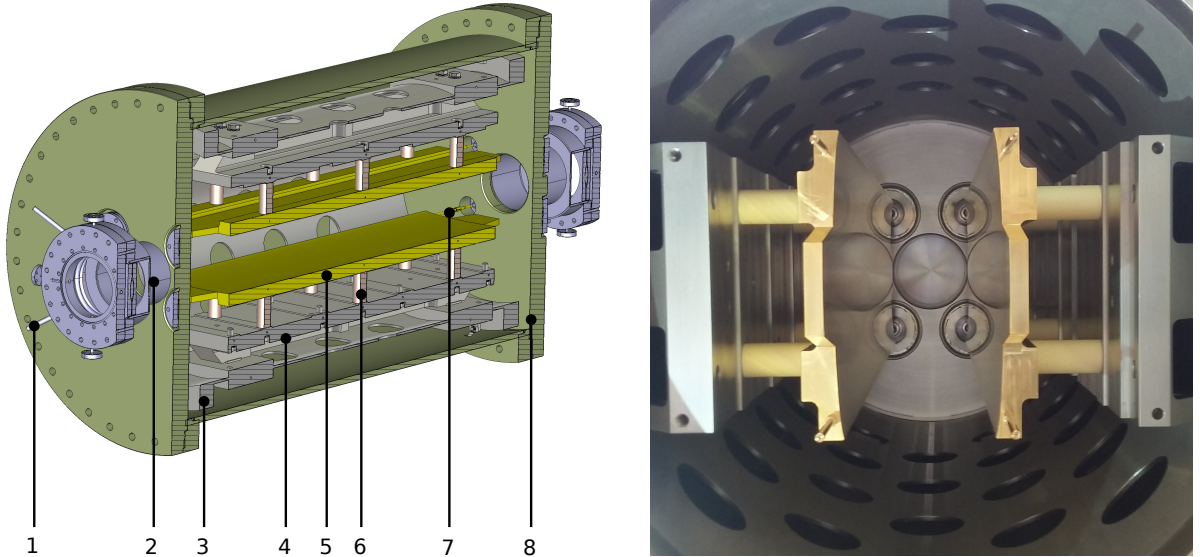
Experiments searching for electric dipole moments (EDMs) of charged particles using storage rings are at the forefront of the incessant quest to find new physics beyond the Standard Model of particle physics. These investigations bear the potential to shed light on the origin of the anomalously large matter-antimatter asymmetry in the Universe (1), for which the combined predictions of the Standard Models of particle physics and of cosmology fall short of the experimentally observed asymmetry by about seven to eight orders of magnitude (2).

In order to cancel out systematic effects in a fully-electric frozen-spin storage ring aiming at a proton EDM sensitivity of  $10^{-29}\text{ e cm}$ , simultaneous measurements of the EDM-driven spin rotations of the counter-propagating beams are necessary. For this purpose, it is imperative to control the relative vertical displacement of two centers of gravity of two beams with an accuracy of about  $5\text{ pm}$  (3). One may wonder whether such an enormously small accuracy value is not prohibited by Heisenberg's uncertainty relation.

Here we report on the measurement of the amplitude of collectively excited vertical oscillations of a deuteron beam orbiting in the magnetic storage ring COSY at a momentum of about 970 MeV/c (4). The data were taken in 2018 in the course of a dedicated experiment in the framework of systematic beam and spin dynamics studies for the deuteron EDM experiment (so-called *precursor* experiment), presently carried out by the JEDI collaboration at COSY (5–7). One of the central devices in the precursor experiment is the radio-frequency (RF) Wien filter (WF), shown in Fig. 1, which was designed to provide a cancellation of the electric and magnetic forces acting on the particle. In this operation mode, the WF affects only the particle spins, but does not perturb the beam orbit (8–10). A slightly detuned WF, however, exerts a non-vanishing Lorentz force on the orbiting beam particles. It is shown that collective beam oscillation amplitudes down to  $1\text{ }\mu\text{m}$  can be detected with the currently available equipment. Our approach to measuring ultra-small displacements complements other measurements of ultra-small forces using different techniques (11–15).

In a storage ring, the beam can be viewed as a rarefied gas of uncorrelated particles. Individual particles are confined vertically in the harmonic oscillator potential. Apart from their conventional individual betatron motions, all the particles participate in one and the same collective and coherent oscillation that is driven by the WF. Therefore, the upper bound of the amplitude of the collective oscillation of the beam corresponds to the upper bound of the oscillation amplitude of a single particle.

From a comparison of the energy of driven transverse beam oscillations to the zero-point energy of a particle in the oscillator potential, it is concluded that the amplitude of the WF-driven single-particle oscillation is only about a factor of ten larger than the quantum limit of Heisenberg’s uncertainty relation. A further improvement of the sensitivity to coherent beam oscillations will become possible when an even more precise adjustment of the driving circuit of the WF (16) will be applied.



(a) CAD drawing of the design of the RF Wien filter. 1: RF feed, 2: beam pipe, 3: inner mounting cylinder, 4: inner support structure, 5: lower electrode, 6: insulator, 7: RF connector, and 8: vacuum vessel.

(b) Photograph with a view along the beam axis showing the gold-plated copper electrodes, which have a length of 808.8 mm.

Figure 1: The waveguide RF Wien filter is mounted inside a cylindrical vessel. The effective length of the device amounts to  $\ell = 1.16$  m. The technical details are described in Refs. (8, 9).

## 2 Principle of the measurement

The Cooler Synchrotron (COSY) (4, 17) at Forschungszentrum Jülich is a storage ring with a circumference of approximately 184 m. Its principal elements used for the experiments are indicated in Fig. 2. For the investigations presented here, the two key devices are the RF WF, based on a parallel-plates waveguide (8), and a conventional electrostatic beam position monitor (BPM) that is used to monitor the beam oscillations (18). The WF generates orthogonal and highly-homogeneous electric and magnetic fields. In the present experiment, the WF was operated in the mode with the electric field pointing vertically upward (in  $y$ -direction), whereas the magnetic field points radially outward (in  $x$ -direction), and the beam moves in  $z$ -direction (see coordinate system in Fig. 2). The effective length of the WF amounts to

$$\ell = 1.16 \text{ m}, \quad (1)$$

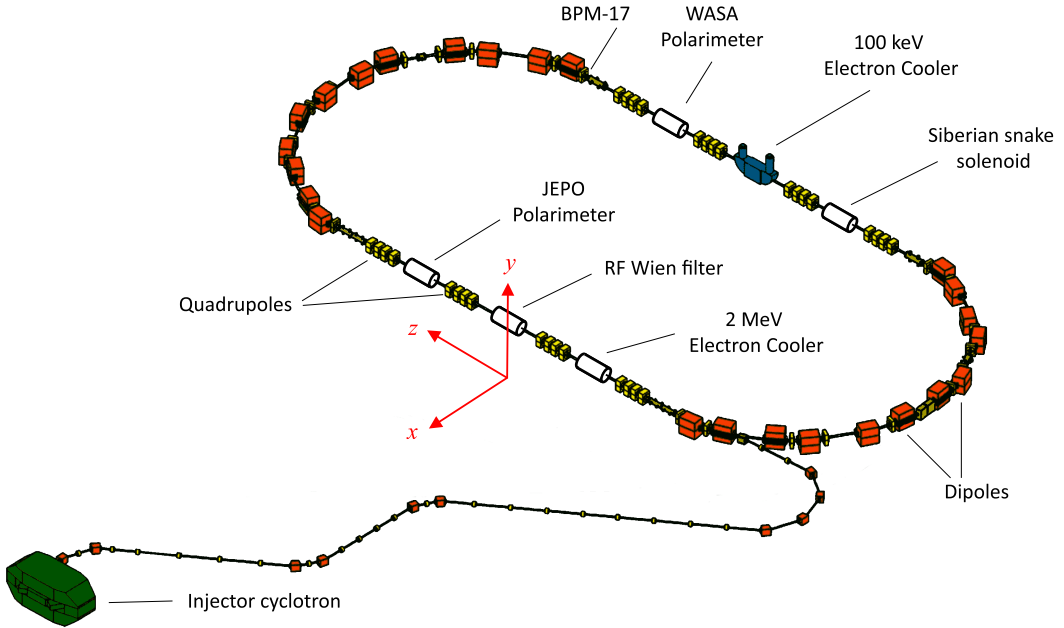


Figure 2: Schematic diagram of the cooler synchrotron and storage ring (COSY) with the main components, especially the focusing/defocussing magnets (quadrupoles) and the bending magnets (dipoles). Indicated are the position of the RF WF and the location of the beam position monitor (BPM 17), used to observe the beam oscillations. Further components such as the 2 MeV electron cooler (19), the WASA (20) and the JEPO (21, 22) polarimeters, and the Siberian snake (23) are also shown. The coordinate system used is indicated.

which corresponds to the length over which the RF fields in the WF can be considered relevant (see Refs. (8, 9) for further technical details).

As a spin rotator for the forthcoming deuteron EDM (precursor) experiment (5–7), the WF is designed to operate in resonance with the spin precession of the orbiting deuterons (8–10, 16), and at a vanishing Lorentz force, given by

$$F_y = q(E_y + v_z \cdot B_x) , \quad (2)$$

where  $q$  denotes the elementary charge and  $v_z$  represents the velocity of the beam particles. Unlike in conventional DC Wien filters, the electric and magnetic fields of the RF WF are

generated *simultaneously* by exciting the transverse electromagnetic (TEM) mode.

When the electric and magnetic fields in the WF are mismatched, *i.e.*, when the electric and magnetic forces no longer cancel each other, the RF fields excite vertical collective beam oscillations at the frequency at which the WF is operated. As already mentioned in the introduction, the collective motion is shared by all particles in the bunch, and the amplitude of the collective beam oscillation is identical to the oscillation amplitude of each individual particle.

With a vanishing Lorentz force, the beam performs idle vertical (and horizontal) betatron oscillations

$$y(t) = y(0) \sqrt{\frac{\beta_y(t)}{\beta_y(0)}} \cos [\psi_y(t)] , \quad (3)$$

where  $\beta_y(t)$  is the betatron amplitude function. With the beam revolution period of  $T = 2\pi/\omega_{\text{rev}}$ , the betatron phase advance  $\psi_y(t)$  satisfies  $\psi_y(t+T) - \psi_y(t) = \omega_y T = 2\pi\nu_y$ , and the vertical betatron tune is given by  $\nu_y = \omega_y/\omega_{\text{rev}}$ .

On the other hand, a mismatched WF generates stroboscopically, *i.e.*, once per turn, a kick of the vertical velocity of the stored particle, given by

$$\Delta v_y(nT) = -\zeta\omega_y \cos(n\omega_{\text{WF}}T) . \quad (4)$$

Here  $n$  denotes the turn number,  $\omega_{\text{WF}}$  denotes the angular velocity of the RF in the WF, and the change  $\Delta y$  of the vertical position  $y$  in the WF is neglected. The amplitude of the velocity change is given by the momentum change accumulated during the time interval  $\Delta t = \ell/v_z$  the particle spends per turn inside the WF,

$$\zeta\omega_y = \frac{F_y \Delta t}{\gamma m} , \quad (5)$$

where  $F_y$  denotes the amplitude of the vertical component of the Lorentz force, and  $\gamma$  and  $m$  are the Lorentz-factor and the mass of the particle, respectively.

In the approximation of a constant amplitude function, the betatron motion can be described in terms of the complex variable  $z = y - iv_y/\omega_y$ , common for the oscillatory motion. With the

initial condition  $z(0) = 0$ , after  $n$  turns, the solution for  $z(n)$  behind the WF reads

$$z(n) = \frac{i\zeta}{2} \cdot \frac{\exp(in\omega_y T) - \exp(in\omega_{WF} T)}{\exp(i(\omega_y - \omega_{WF})T) - 1} + \{\omega_{WF} \rightarrow -\omega_{WF}\}. \quad (6)$$

This expression serves as the initial condition for the idle betatron motion during the subsequent  $(n + 1)$  turn. Driven by the mismatched WF, all beam particles participate in one and the same collective and coherent oscillation, and according to Eq. (6), the beam oscillates at the WF frequency  $\omega_{WF}$ . A lock-in amplifier may be used to selectively measure the corresponding Fourier component of the beam oscillation  $y = \epsilon_y \cos(n\omega_{WF}T)$  from the output of a BPM. Its amplitude is given by

$$\epsilon_y = \frac{\zeta}{2} \cdot \frac{\sin(2\pi\nu_y)}{\cos(2\pi\nu_{WF}) - \cos(2\pi\nu_y)}, \quad (7)$$

where the vertical betatron tune is given by  $\nu_y = \omega_y/\omega_{rev}$  and the WF tune by  $\nu_{WF} = \omega_{WF}/\omega_{rev}$ .

When the WF tune is close to the vertical betatron tune, a resonant enhancement of the beam oscillation amplitude  $\epsilon_y$  occurs. Equation (7) describes Hooke's law,  $F_y = k_H \epsilon_y$ , and Hooke's constant is given by

$$k_H = \left| \frac{2\gamma m \omega_y}{\Delta t} \cdot \frac{\cos(2\pi\nu_{WF}) - \cos(2\pi\nu_y)}{\sin(2\pi\nu_y)} \right|. \quad (8)$$

We compare the measured amplitude of the WF driven oscillations to the amplitude  $Q$  of the zero-point betatron oscillations with energy  $\hbar\omega_y/2$ , which entails  $Q^2 = \hbar/(m\gamma\omega_y)$ . For the present experiment, we obtain

$$Q = \frac{82}{\sqrt{\gamma\nu_y}} \text{ nm}. \quad (9)$$

With the actual COSY values for the betatron tune  $\nu_y$  and the Lorentz-factor  $\gamma$  of the beam (see Table 1, Appendix A), the quantum limit of the vertical oscillations, driven by the WF, amounts to

$$Q \approx 41 \text{ nm}. \quad (10)$$

The interpretation of the measured oscillation amplitudes in terms of the WF parameters requires numerical simulations of the performance of the WF as an element of the storage

ring (8). The details relevant to the present study are described below; the corresponding beam simulations carried out are consistent with the available experimental results on the properties of COSY (24).

### 3 Operation of the RF Wien filter

The control of the Lorentz force of the waveguide RF Wien filter is based on the wave-mismatch principle (10). An impedance mismatch is introduced at the load part of the device to deliberately create reflections that generate a standing wave pattern inside the WF (16). These standing waves can be represented by the complex-valued field quotient  $Z_q$ , defined as the ratio of the total electric to the total magnetic field strength,

$$Z_q = \frac{E^{\text{total}}}{H^{\text{total}}} = \frac{E^+ + E^-}{H^+ - H^-} = \frac{E^+ + \Gamma \cdot E^+}{H^+ - \Gamma \cdot H^+} = Z_w \frac{1 + \Gamma}{1 - \Gamma} = Z_0 \frac{d}{W} \frac{1 + \Gamma}{1 - \Gamma}, \quad (11)$$

where the superscripts '+' and '−' refer to the forward and backward direction of propagation,  $Z_w$  is the wave impedance,  $Z_0 \approx 377 \Omega$  is the vacuum wave impedance,  $d = 100 \text{ mm}$  is the distance between the electrodes,  $W = 182 \text{ mm}$  is their width (8), and  $\Gamma$  is the reflection coefficient that controls the amplitude and phase of the reflected wave. During the measurements described here, the WF was typically operated at a net input RF power of 600 W.

The field quotient  $Z_q$  is controlled via a specially designed RF circuit (16). By altering  $\Gamma$  via two variable vacuum capacitors, called  $C_L$  and  $C_T$ , a wide range of  $Z_q$  values can be covered, and the matching point corresponding to the minimum induced vertical beam oscillation amplitude may be determined.

### 4 Measurement of the beam oscillations

In this experiment, the electric field of the WF is oriented vertically and the magnetic field horizontally. This implies that the oscillations mainly take place along the  $y$ -axis [see Eq. (2)]. For

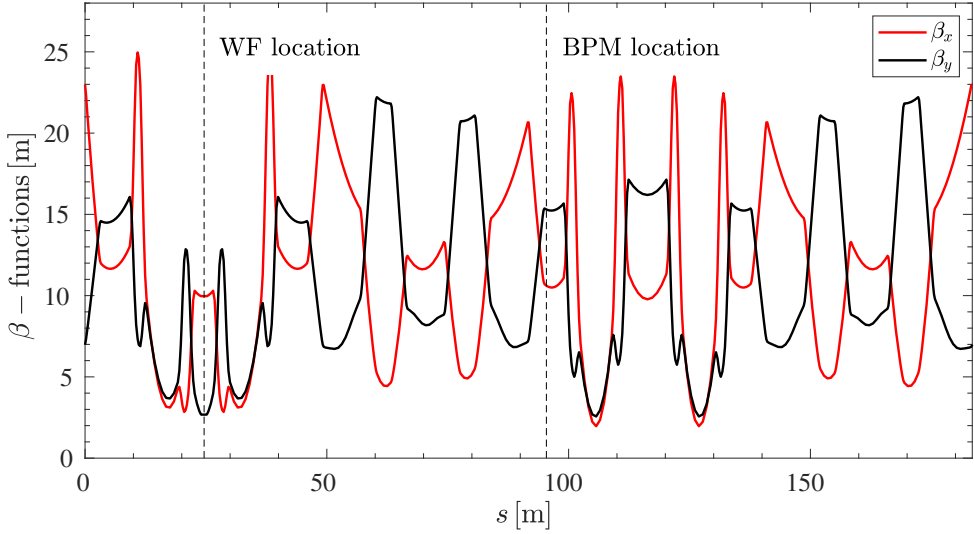


Figure 3: Vertical and horizontal beta-functions along the circumference of COSY (24). The vertical dashed lines mark the location of the WF and of the BPM used during the measurement of the beam oscillations.

the detection of the vertical beam oscillations, a conventional beam position monitor (BPM) has been employed. In order to be most sensitive, BPM 17 located in the straight section opposite to the WF (see Fig. 2) with a large vertical  $\beta$  function was used,  $\beta_y^{\text{BPM}} \approx 15.3049$  m, while at the WF location,  $\beta_y^{\text{WF}} \approx 2.6784$  m, as shown in Fig. 3. The arguments to pick BPM 17 are further discussed below in Sec. 4.1.

In order to measure small beam oscillations, a technique based on lock-in amplifiers<sup>1</sup> was developed (25). These devices operate in the frequency domain and lock onto a signal whose frequency is set as a reference, which is particularly useful in an electromagnetically noisy environment. Each measurement consisted of two subsequent machine cycles of 3 min duration, as depicted in Fig. 14 in Appendix B.

A stored beam bunch circulating at a revolution frequency of  $f_{\text{rev}}$  that passes through a BPM induces a voltage signal on all its four electrodes, as indicated in the BPM readout scheme,

<sup>1</sup>HF2LI 50 MHz Lock-in Amplifier, Zurich Instruments AG, 8005 Zurich, Switzerland, <https://www.zhinst.com/others/products/hf2li-lock-amplifier>.

<sup>2</sup>Experimental Physics and Industrial Control System, <https://epics.anl.gov/index.php>.

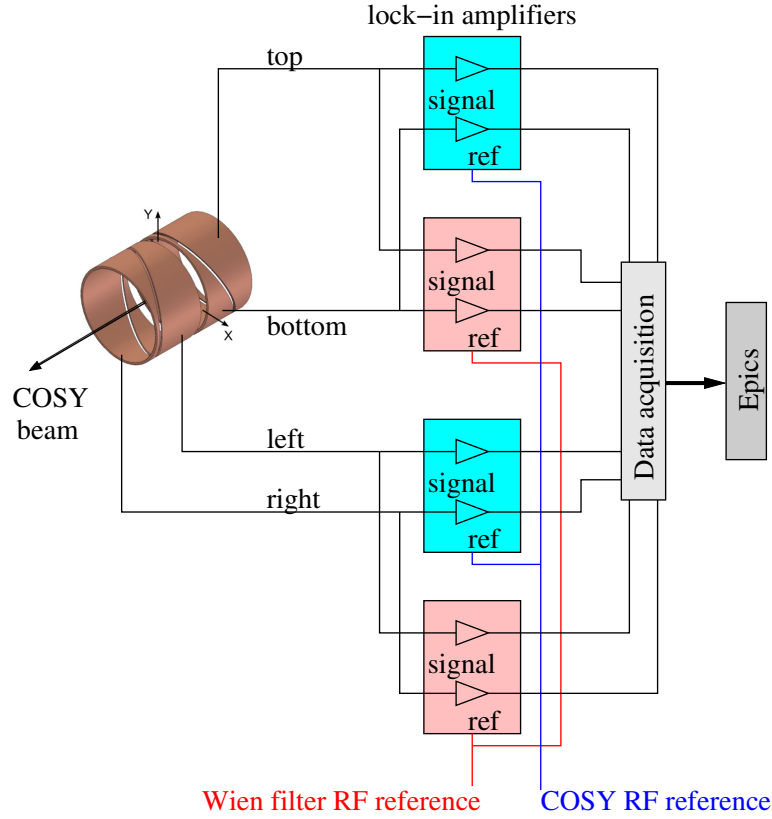


Figure 4: Readout scheme of the COSY BPM 17. The signals of the four electrodes are fed into lock-in amplifiers. The differential signal of each electrode is analyzed at the two reference frequencies given by the COSY RF and the Wien filter frequency. The resulting Fourier amplitudes of the signals are recorded in the EPICS<sup>2</sup> archiving system of COSY.

shown in Fig. 4. For the detection of vertical beam oscillations, only the voltage signals  $U_{t,b}$  from the top (t) and bottom (b) electrodes are considered. These signals are trains of short pulses with the repetition frequency  $f_{\text{rev}}$ . In view of Eq. (3) and as far as the Fourier spectrum of the beam oscillations is concerned, without loss of generality the BPM can be considered to be located right behind the WF, and the induced voltages can be represented by

$$U_{t,b} = [U_0 \pm \Delta U(\Delta y)] \cos(\omega_{\text{rev}} t), \quad (12)$$

where the index "t" refers to the + sign and the index "b" to the - sign, respectively. Here,  $U_0$  denotes the voltage induced when the beam passes exactly through the center of the BPM,

and  $\Delta U(\Delta y)$  represents the voltage variation induced by a beam that is vertically displaced by  $\Delta y$ . The harmonic factor  $\cos(\omega_{\text{rev}}t)$  describes the pulse repetition frequency, and  $\cos(\omega_{\text{rev}}t) = 1$  applies to multiples of the orbital period  $t = nT$ .

For small beam displacements, the BPM operates in its linear regime, which implies that the induced voltages take the form

$$\Delta U(\Delta y) = \kappa \cdot \Delta y \cdot U_0, \quad (13)$$

where  $\kappa$  is a calibration factor that needs to be determined. At a momentum of 970 MeV/c, the revolution frequency of deuterons orbiting in COSY is  $f_{\text{rev}} \approx 750$  kHz. The WF is operated at the  $k^{\text{th}}$  sideband of the spin-precession frequency, given by

$$f_{\text{WF}} = \frac{\omega_{\text{WF}}}{2\pi} = (k + \nu_s)f_{\text{rev}} = k \cdot f_{\text{rev}} + f_s. \quad (14)$$

Here  $\nu_s = G\gamma$  denotes the spin tune, *i.e.*, the number of spin precessions per revolution,  $G \approx -0.1430$  is the magnetic anomaly of the deuteron, and the spin precession frequency  $f_s = \nu_s f_{\text{rev}}$  (8). It should be noted that the beam oscillations do not depend on the actual choice of the sideband. In the present experiment the WF was operated at  $k = -1$ , which corresponds to  $f_{\text{WF}} \approx 871$  kHz<sup>2</sup>.

The induced oscillations of amplitude  $\epsilon_y$  contribute to Eq. (12) the harmonic voltage variation  $\Delta U(y(t))$ . The BPM in conjunction with the lock-in amplifiers is used to measure at times  $t = nT$  the beam positions at the reference frequencies, *i.e.*, at  $f_{\text{WF}}$  and at  $f_{\text{rev}}$ . Given that  $y(t)$  can be evaluated at the spin precession frequency, the BPM signals of the upper and lower electrodes can be written as follows

$$\begin{aligned} U_{\text{t,b}}(t) &= [U_0 \pm \Delta U(\Delta y) \pm \Delta U(y(t))] \cos(\omega_{\text{rev}}t), \\ &= [U_0 \pm \Delta U(\Delta y) \pm \kappa \epsilon_y U_0 \cos(\omega_s t)] \cos(\omega_{\text{rev}}t), \\ &= [U_0 \pm \kappa \Delta y U_0] \cos(\omega_{\text{rev}}t) \pm \frac{1}{2} \kappa \epsilon_y U_0 \cos(\omega_{\Delta} t) \pm \frac{1}{2} \kappa \epsilon_y U_0 \cos(\omega_{\Sigma} t). \end{aligned} \quad (15)$$

---

<sup>2</sup>For the considerations presented in this paper, negative and positive frequencies are considered equivalent.

Here  $\omega_\Delta$  and  $\omega_\Sigma$  represent sidebands of the WF frequency at

$$\begin{aligned}\omega_\Delta &= \omega_{\text{rev}} - \omega_s = \omega_{\text{WF}}|_{k=1}, \text{ and} \\ \omega_\Sigma &= \omega_{\text{rev}} + \omega_s = \omega_{\text{WF}}|_{k=-1}.\end{aligned}\tag{16}$$

In order to measure the beam oscillations, four lock-in amplifiers (25) were used, two for the horizontal and two for the vertical direction. For each direction, one lock-in amplifier detects the Fourier amplitudes at  $f_{\text{rev}} \approx 750$  kHz and a second one at  $f_\Sigma = f_{\text{rev}} + f_s \approx 871$  kHz. The lock-in amplifiers receive reference frequencies from the signal generator of the WF and from the master oscillator of COSY. The four Fourier amplitudes of the top and bottom electrodes are determined practically in real-time, yielding

$$\begin{aligned}A_{t,b}^{\text{rev}} &= U_0 \pm \kappa \Delta y U_0, \text{ and} \\ A_{t,b}^\Sigma &= \mp \frac{1}{2} \kappa \epsilon_y U_0.\end{aligned}\tag{17}$$

The amplitude of the vertical oscillation  $\epsilon_y$  can then be determined from

$$\frac{A_t^\Sigma - A_b^\Sigma}{A_t^{\text{rev}} + A_b^{\text{rev}}} = \hat{\epsilon}_y = \kappa \frac{U_0}{2U_0} \epsilon_y = \frac{1}{2} \kappa \epsilon_y.\tag{18}$$

The uncalibrated raw asymmetry of the four Fourier amplitudes is denoted by  $\hat{\epsilon}_y$ . The determination of the calibration constant  $\kappa$ , required to calibrate the vertical oscillation amplitude, is described in detail in Appendix B. It amounts to

$$\kappa = (5.82 \pm 0.43) \cdot 10^{-6} \mu\text{m}^{-1}.\tag{19}$$

During the experiments, the vertical betatron tune of the machine amounted to about  $\nu_y \approx 3.6040$ .<sup>3</sup> The frequency  $f_\Sigma \approx 871$  kHz, at which the WF is operated, is well separated from the lowest intrinsic spin resonances<sup>4</sup> at 297 kHz, 453 kHz, 1048 kHz, and 1204 kHz.

---

<sup>3</sup>The numerical values used for the simulation calculations are listed in Table 1 of Appendix A.

<sup>4</sup>An intrinsic depolarizing resonance is encountered, when the betatron motion of the particles is in sync with the spin motion, hence, when the condition  $f_s = \nu_s f_{\text{rev}} = f_y = (nP \pm \nu'_y) f_{\text{rev}}$  is fulfilled (26), where  $n \in \mathbb{N}$ ,  $P$  denotes the superperiodicity of the lattice, and  $\nu'_y$  the fractional tune. During the experiments described here,  $P = 1$  (see also Fig. 3).

The two variable and highly accurate capacitors,  $C_L$  and  $C_T$ , are driven by stepper motors. They constitute the main dynamical elements of the driving circuit. Each pair of capacitor values yields a well-defined field quotient  $|Z_q|$ , as shown in Fig. 5 (a). Away from the matching point, a phase shift  $\angle Z_q$  occurs between electric and magnetic fields, as shown in Fig. 5 (b). The corresponding Lorentz force leads to the measured beam oscillations, *i.e.*, the function  $\epsilon_y = f(C_L, C_T)$ , which can be visualized in the form of a 2D map, as shown in Fig. 6. The experimental data were taken on a grid of  $(7 \times 6)$  points of  $C_L$  and  $C_T$ , with corresponding grid spacings of  $(94.5 \pm 1.0)$  pF for  $C_L$  and  $(95.8 \pm 1.0)$  pF for  $C_T$ . Each grid spacing corresponds to 1000 steps of the corresponding stepper motors. The calibration of the capacitances  $C_L$  and  $C_T$  as a function of step number is discussed in detail in (16). The grid spans over  $C_L \in [318.88, 885.58]$  pF and  $C_T \in [428.99, 907.79]$  pF. The uncertainties of the grid spacings are systematic ones.<sup>5</sup> It should be emphasized that the technique of inducing collective beam oscillations can be used later in the actual EDM experiments as a tool to investigate the systematic effects of beam oscillations.

The map of the measured and calibrated vertical beam oscillations  $\epsilon_y$  is shown in Fig. 6. The parameters of the matching point are given by

$$\begin{aligned} C_L &= (697.1 \pm 1.0) \text{ pF, and} \\ C_T &= (503.0 \pm 1.0) \text{ pF,} \end{aligned} \tag{20}$$

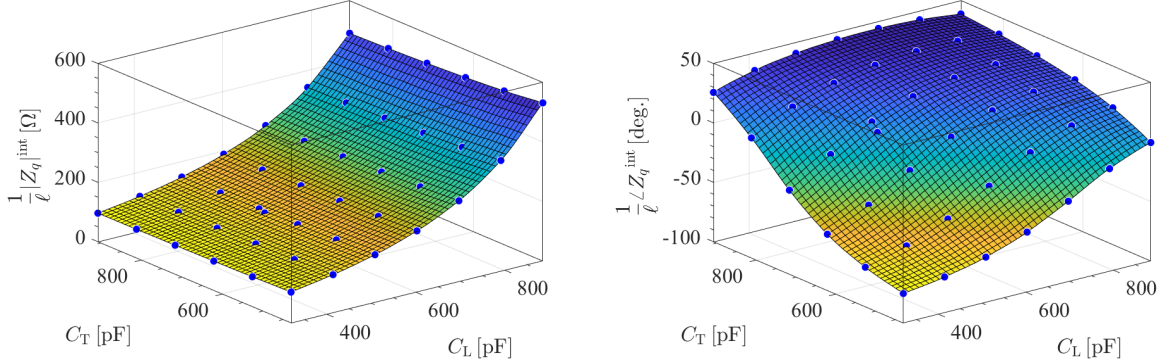
and the corresponding minimal beam oscillation amplitude at the location of BPM 17 amounts to

$$\epsilon_y^{\min} = (1.1 \pm 0.5) \mu\text{m}. \tag{21}$$

The maximum measured amplitude of driven beam oscillations at a strongly mismatched point

---

<sup>5</sup>The individually measured uncertainties of the capacitors are actually much smaller than the stated uncertainty of 1.0 pF. However, other factors, such as the capacitances and inductances of the connectors and cables and their power dependencies, also contribute to the aforementioned uncertainties.



(a) Magnitude of the field quotient  $|Z_q|$ , evaluated integrally, where  $|Z_q|^{\text{int}} = \int |Z_q| d\ell$ . Ideally, with  $|Z_q|$  close to 176  $\Omega$ , the electric and magnetic forces are equal. (b) Phase of the field quotient  $\angle Z_q$  evaluated integrally, where  $\angle Z_q^{\text{int}} = \int \angle Z_q d\ell$ . A non-vanishing  $\angle Z_q$  implies a phase shift between the electric and magnetic fields.

Figure 5: Simulated *integral* magnitude (a) and phase of the field quotient  $Z_q$  (b) at each point of the  $C_L$  and  $C_T$  grid, indicated by the blue points,  $\ell$  denotes the effective length of the WF [see Eq. (1)]. Besides the matching point [see Eq. (20)],  $(7 \times 6)$  grid points were investigated.

with 600 W of input RF power amounts to

$$\epsilon_y^{\max} = (66.2 \pm 3.1) \mu\text{m}. \quad (22)$$

In Fig. 7 (a), the data measured at the matching point [Eq. (20)] are shown. Each sample was recorded by the lock-in amplifiers with an integration time set to 0.5 s, corresponding to an average of 5000 measurements. A Monte Carlo error propagation model was applied to treat the uncertainties of the still uncalibrated raw position asymmetries  $\hat{\epsilon}_y$  and the calibration coefficient  $\kappa$  (27). The results are fitted with a normal distribution, as shown in Fig. 7 (b), from which the mean value  $\mu_{\epsilon_y}$  and the error of the measured beam oscillations  $\sigma_{\epsilon_y}$  are estimated. The latter represents the *systematic* error of the measurement. It should be noted that the map shown in Fig. 6 is actually a function of *all* the circuit elements. The uncertainties of  $\epsilon_y$  are influenced by the uncertainties of all circuit elements and also by the ones of the BPM itself, which include its readout electronics, *i.e.*, the lock-in amplifiers.

To appreciate the result given in Eq. (21), one can compare the oscillation amplitude to the

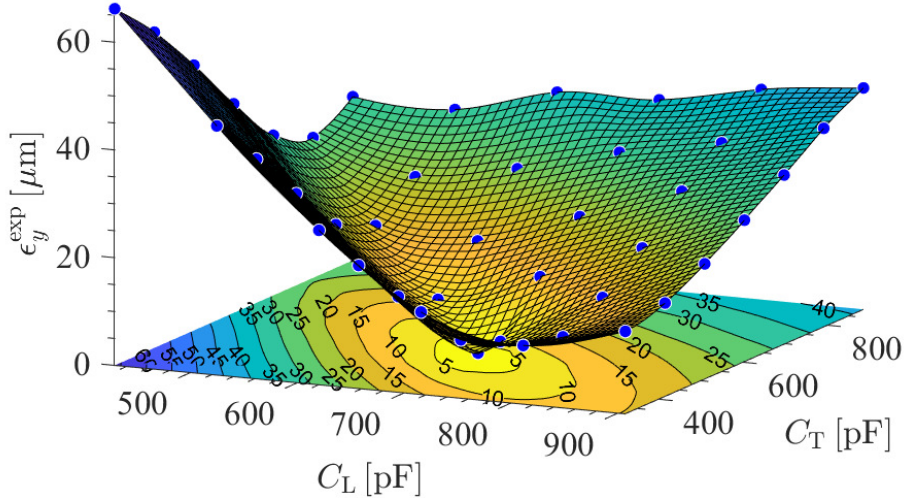
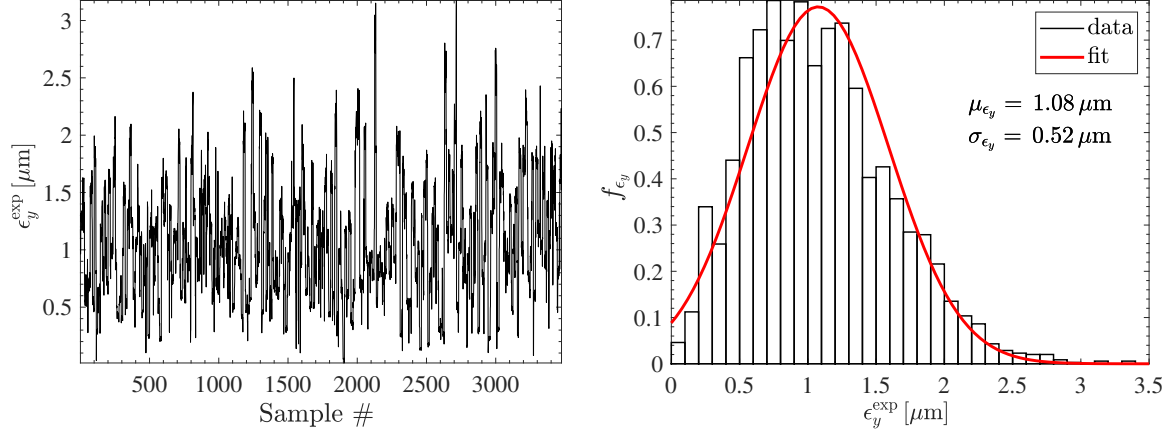


Figure 6: Measured amplitudes of beam oscillations  $\epsilon_y^{\text{exp}}$  at BMP 17, plotted on a grid as a function of the variable capacitor values  $C_L$  and  $C_T$ . To avoid crowding up the map, the error bars of the data points were omitted, these are shown in Fig. 13 instead. The parameters of the matching point are given in Eq. (20).

$1\sigma$  vertical beam size. The latter has been deduced from the  $1\sigma$  beam emittance  $\epsilon_y^b$  and the amplitude of the  $\beta$  function at the BPM position, yielding

$$\sigma_y^{\text{BPM}} = \sqrt{\beta_y^{\text{BPM}} \epsilon_y^b} \approx 1.4 \text{ mm} . \quad (23)$$

Although in the present experiment the beam emittance was not monitored, as a reference value for a well-cooled beam in the above numerical estimate of  $\sigma_y^{\text{BPM}}$ , the experimental result for the  $2\sigma$  beam emittance of 49.3 MeV protons in COSY,  $\epsilon_y^b = (0.92 \pm 0.15) \mu\text{m}$  (24), has been rescaled to the conditions of the present experiment. It is noteworthy that with the present equipment it is possible to access coherent beam oscillations with amplitudes that are more than three orders of magnitude smaller than the beam size.



(a) Measured oscillation amplitudes  $\epsilon_y$  using data samples of 0.5 s duration, each sample reflects the average of 5000 measurements of the lock-in amplifiers.

(b) Probability density distribution  $f_{\epsilon_y}$  of the measured data, fitted with a Gaussian to determine mean and standard deviation.

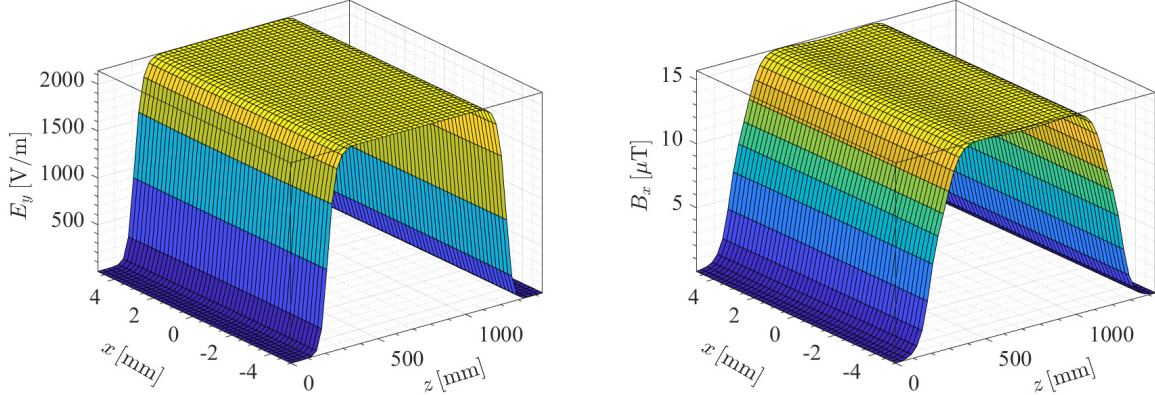
Figure 7: Measured beam oscillations at the matching point [Eq. (20)] of the map shown in Fig. 6. The samples shown in panel (a) were acquired during a data taking period of 108 min, using 36 machine fills (cycles).

## 4.1 Beam dynamics simulations

To improve our understanding of the measured results, a computer code was developed to model the beam dynamics in the COSY storage ring. The modeled storage ring consists of a sequence of drift regions, quadrupole and dipole magnets, the WF, and BPMs. These elements are represented by transfer matrices, which are well understood and documented in the literature (28). In the model of the ring, the actual settings of the beam optics elements of COSY were those used at the time when the experiment took place. Simulations are based on the Hamiltonian formulation as presented in Ref. (28). The WF is modeled by a time-dependent matrix that also takes into account the arrival time of the particles.

In order to be able to perform reliable beam simulations, we have placed great emphasis on good spatial resolution and the accuracy of the 3D field maps inside the WF<sup>6</sup>, computed using

<sup>6</sup>Each field map consists of  $2 \cdot 10^6$  points, 200 points along the  $x$  axis ( $x \in [-5 \text{ mm}, 5 \text{ mm}]$ ), 200 points along the  $y$  axis ( $y \in [-5 \text{ mm}, 5 \text{ mm}]$ ), and 50 points along the  $z$  (WF) axis ( $z \in [-\ell/2, +\ell/2]$ ), where  $\ell$  is specified in



(a) 3D electric field distribution of the component  $E_y$ . (b) 3D magnetic field distribution of the flux density component  $B_x$ .

Figure 8: Examples of the main electric and magnetic field components inside the waveguide RF Wien filter at the matching point [see Eq. (20)] with an input RF power of 600 W. The electric field component in (a) points vertically upward ( $y$ -direction), while the component of the magnetic flux density in (b) points radially outward ( $x$ -direction).

a 3D electromagnetic simulation tool<sup>7</sup>. The fringe fields of the WF are included, because they are of particular importance for the beam oscillations, as will be discussed later. An example of the computed 3D fields of the WF at the experimentally determined matching point is shown in Fig. 8. The beam-tracking simulations use the three vector components of the electric and magnetic fields. The Wien filter is implemented as an RF kicker, as described by Eq. (4).

Inside COSY there are 32 BPMs available to control the horizontal and vertical beam position during operation. In order to select one of them with a good sensitivity to determine the beam oscillations induced by the WF, a number of particles were tracked, as described above, and the orbit response induced by a field change at the location of the WF was calculated at each BPM location<sup>8</sup>. As a result, BPM 17, located about 70 m downstream of the WF (see Fig. 2),

Eq. (1).

<sup>7</sup>Electromagnetic and circuit simulations were performed using CST, from Dassault Systèmes, Vélizy-Villacoublay, France, <https://www.3ds.com>.

<sup>8</sup>In the preparatory stage, simulations were carried out using the Software Toolkit for Charged-Particle and X-Ray Simulations BMAD (29).

was chosen because it offered good sensitivity to both radial and vertical beam oscillations.

Figure 8 shows the main field components  $E_y$  and  $B_x$ . When mismatched, the WF generates periodic transverse perturbations of the trajectory as a result of the velocity kicks in the form of beam oscillations. Switching off the WF eliminates such oscillations. The maximum amplitude of the observed oscillations in the simulation is then used to represent  $\epsilon_y$ . The two simulated vertical beam oscillation amplitudes of BPM 17 and WF read

$$\begin{aligned}\epsilon_y^{\text{BPM}} &= (1.086 \pm 0.082) \text{ } \mu\text{m}, \text{ and} \\ \epsilon_y^{\text{WF}} &= (0.435 \pm 0.031) \text{ } \mu\text{m}.\end{aligned}\tag{24}$$

A detailed description of the determination of the uncertainties of the beam simulations is discussed in the next section.

For each and every *measured* point on the  $C_L$  versus  $C_T$  grid, a beam dynamics simulation was carried out. For each of these points, a 3D field map of the WF was generated and then used for the beam tracking simulations. The results of these simulations are shown in Fig. 9, and are later compared with the results of the measurements.

## 4.2 Evaluation of the uncertainties of beam simulations

The accuracy with which the Lorentz force and the resulting amplitudes of the beam oscillations can be tuned depends on the accuracy with which the field quotient  $Z_q$  can be *integrally* set to the desired value.  $Z_q$  depends on the hardware elements in the driving circuit. In order to evaluate the effects of uncertainties of these elements, extensive coupled circuit electromagnetic simulations have been conducted, as discussed in Ref. (16). The uncertainties involved are listed in Table 6 and shown in Fig. 16 of Ref. (16). As far as the Lorentz force is concerned, most important are the uncertainties of the fixed inductance  $L_f$  and the fixed resistance  $R_f$ . Once these uncertainties are known, one can compute the electric and magnetic fields and the corresponding Lorentz force, *including* their corresponding errors. Figure 10 shows a few examples of the main

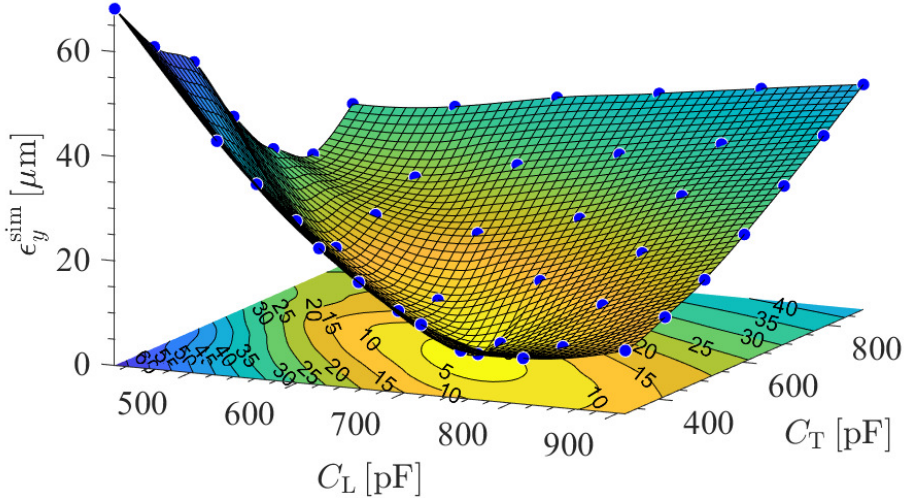
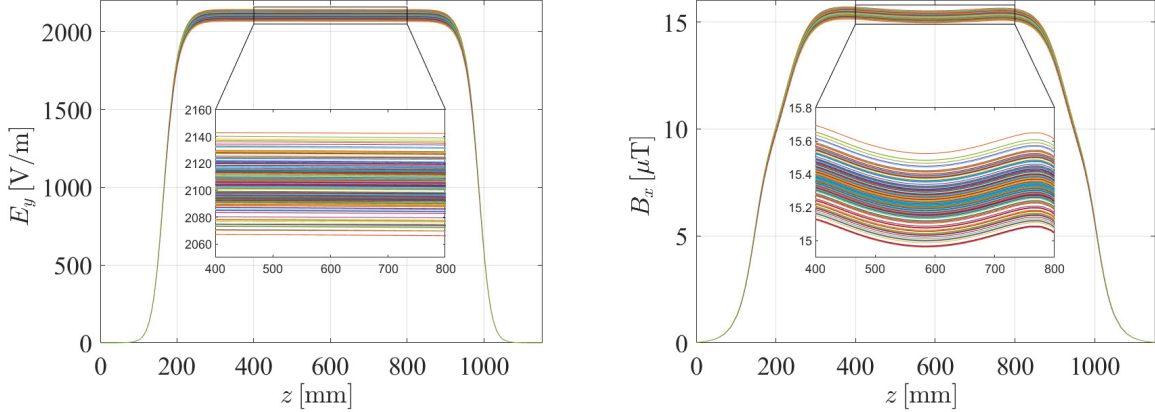


Figure 9: Simulated amplitudes of beam oscillations  $\epsilon_y^{\text{sim}}$  as a function of the variable capacitor values  $C_L$  and  $C_T$ . To avoid overcrowding the map, the error bars of the data points were omitted here and are shown in Fig. 13.

components of the electric and magnetic fields, computed with the above mentioned circuit uncertainties. As will be explained below, these 3D fields, together with their uncertainties, are subsequently used as input to the beam simulations.

The algorithm used to compute the uncertainties of the beam simulations is the polynomial chaos expansion (PCE), as explained in Refs. (9, 16) and in Appendix C. The PCE has been proven in many applications in science and engineering to be just as accurate as the computationally much more expensive Monte-Carlo counterpart (9, 30–32).

To compute the uncertainties  $\sigma_{\epsilon_y}$ , the PCE algorithm requires a random set of the simulated  $\epsilon_y$ , alongside a set of randomized input parameters according to their uncertainties to generate the output. The set of  $\epsilon_y$  is produced using a number of beam-tracking simulations, where for each instance, a 3D field map of the WF is generated, according to the randomized input parameters. An example of the electric and magnetic fields evaluated at the center of the WF

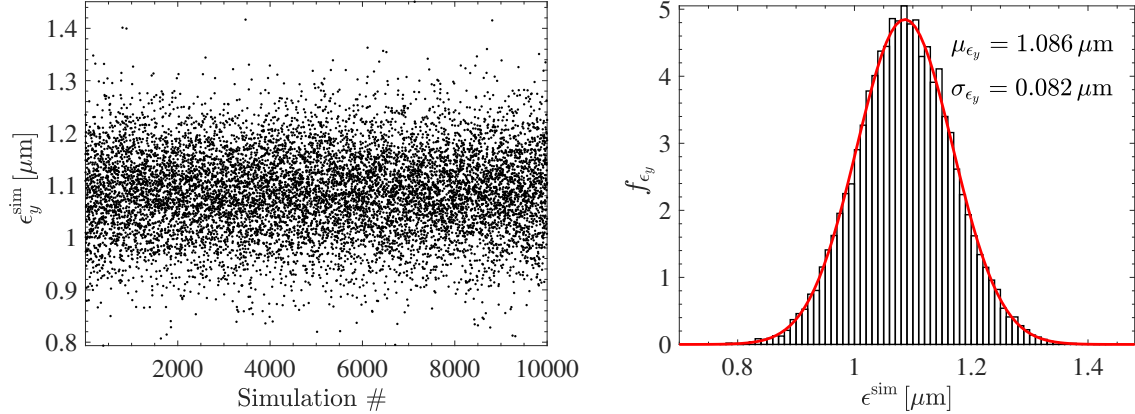


(a) Electric field component  $E_y(z)$  under circuit uncertainties. (b) Magnetic field component  $B_x(z)$  under circuit uncertainties.

Figure 10: 200 examples of the electric and magnetic fields as a function of  $z$  along the beam axis under the circuit uncertainties, specified in the list of uncertainties in Table 6 of (16).

for the matching case [see Eq. (20)] is shown in Fig. 10. The magnitudes of the fields vary as a function of the uncertainties of the driving circuit (16). The numerical tracking of the particles through these fields generates a collection of different  $\epsilon_y$  values that the PCE algorithm can use to project the output onto orthogonal polynomial functions. These functions serve as basis functions, from which the expansion coefficients are determined that are used to generate a large sample of outputs to compute the uncertainties of the beam simulations.

In Fig. 11 (a), the simulated values of  $\epsilon_y$  are shown for the matching case. The detailed steps to achieve this result are discussed in Appendix C. As shown in Fig. 11(b), fitting these data to a Gaussian yields a standard deviation of  $\sigma_{\epsilon_y} = 0.082 \mu\text{m}$ . This number is of considerable importance, because, given the uncertainties of the driving circuit, it sets the lower limit that can be achieved by minimizing the amplitude of the vertical beam oscillations when more sharply tuning the driving circuit of the WF. The same procedure is performed on each point of the map shown in Fig. 9.



(a) Simulated oscillation amplitudes under uncertainties at the matching point (Eq. (20)). Of the  $10^6$  simulations that were carried out, only  $10^4$  are shown here.

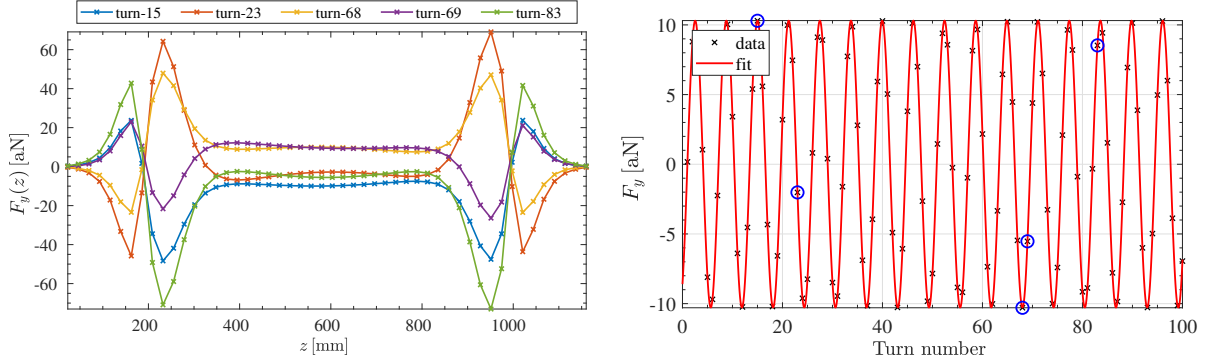
(b) Probability density distribution  $f_{\epsilon_y}$  of the  $10^6$  simulations from panel (a), fitted by a Gaussian to determine mean and standard deviation.

Figure 11: Results of the sparse PCE algorithm to compute the uncertainties of the simulated vertical beam oscillations at BPM 17.

### 4.3 Interpretation of the results

The simulations yield the net Lorentz force exerted by the WF on beam particles and the corresponding oscillation amplitudes for each measured point of the  $C_L$  versus  $C_T$  map, shown in Fig. 6. The only variables in this case are the field maps of the WF itself. After 1000 turns, the beam position is computed at the same location in the ring, where the measurement using BPM 17 took place (see Fig. 2). The net Lorentz force is a result of local cancellations between the electric and magnetic field components, as illustrated in Fig. 12 for the matching point given in Eq. (20) with the minimal measured oscillation amplitude.

In Fig. 12(a), the *local* Lorentz force is shown along the trajectory for 5 randomly chosen passes through the WF. The trajectory of the same particle changes from pass to pass, thereby different WF fields and consequently different values of the Lorentz force  $F_y$  will be picked up. As shown in Fig. 12, even at the matching point, the matching is still imperfect, and the largest local  $F_y$  contributions are caused by the fringe fields at the entrance and exit of the WF. Despite the different location of the particle in the vertical and horizontal phase space



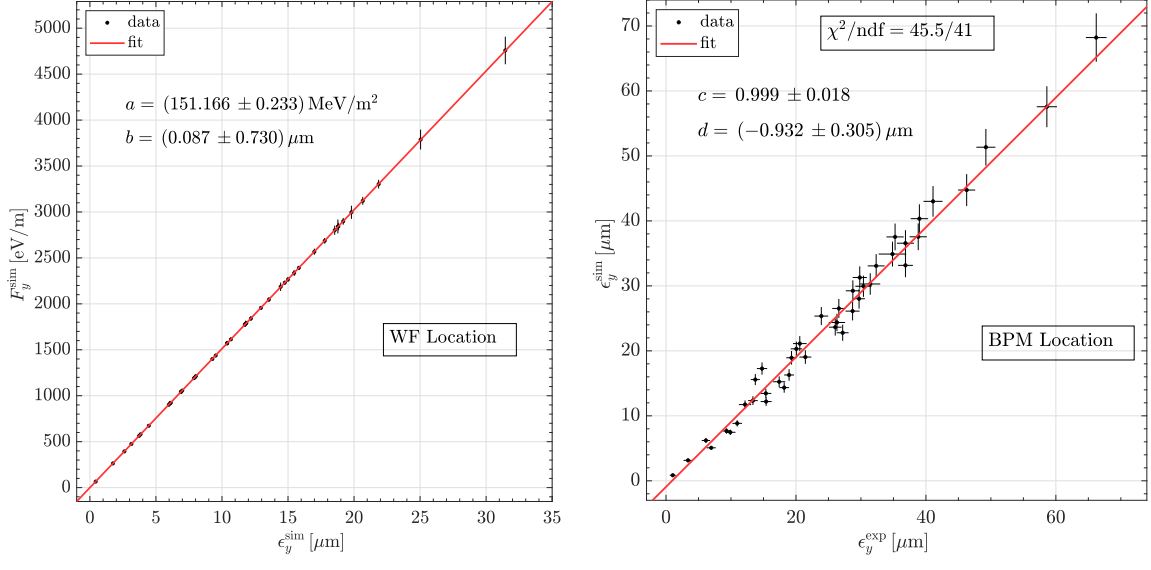
(a) Local Lorentz force  $F_y(z)$  exerted on a single deuteron for different passes through the WF. The turn numbers used here were randomly selected between 1 to 100. The fields were evaluated at the crosses and the interconnecting lines are to guide the eye.

(b) Integral Lorentz force  $F_y(n)$  evaluated along the trajectory. Each point represents an overall kick exerted per turn  $n$ . The points marked in blue correspond to the integrated local Lorentz force of the individual turns shown in panel (a).

Figure 12: Simulation of the local and integrated Lorentz force in the WF at the matching point of Eq. (20). Depending on the initial coordinates in the vertical and horizontal phase space, the particle travels along different trajectories, and therefore picks up different field components  $F_y$ .

at the entrance of the WF upon subsequent passes, the integration of these local forces along the particle trajectories exhibits nevertheless a perfectly harmonic time dependence with the frequency  $f_s$ , as shown in Fig. 12(b). The points encircled in blue correspond to the randomly selected passes through the WF, shown in Fig. 12(a).

In the left panel of Fig. 13, the amplitude of the simulated Lorentz force  $F_y^{\text{sim}}$  is plotted versus the simulated oscillation amplitude  $\epsilon_y^{\text{sim}}$  at the WF position. As expected, it exactly follows Hooke's law with a spring constant of  $k_H = (151.2 \pm 0.2) \text{ MeV/m}^2$ . In Fig. 13(b), the measured amplitudes are compared with the ones simulated for the location of BPM 17. The two sets  $\epsilon_y^{\text{exp}}$  and  $\epsilon_y^{\text{sim}}$  are in very good agreement with each other. The horizontal and vertical error bars are derived from the uncertainties of the measurements and simulations, represented by the width of the distributions, as shown in Figs. 10(b) and 7(b). It is important to note that the error bars refer to *systematic uncertainties* and should not be confused with statistical ones. This implies that repetitions of either the measurements or the simulations will neither reduce



(a) Simulated Lorentz force  $F_y^{\text{sim}}$  at the WF location as function of the simulated beam oscillation amplitudes  $\epsilon_y^{\text{sim}}$ , fitted with the function  $F_y^{\text{sim}} = a \cdot \epsilon_y^{\text{sim}} + b$ .

(b) Simulated beam oscillation amplitude  $\epsilon_y^{\text{sim}}$  versus the measured oscillation amplitude  $\epsilon_y^{\text{exp}}$  at the BPM, fitted with the function  $\epsilon_y^{\text{sim}} = c \cdot \epsilon_y^{\text{exp}} + d$ .

Figure 13: (a): Simulated amplitude of the Lorentz force at the WF location as function of the simulated beam oscillation amplitudes  $\epsilon_y^{\text{sim}}$ . (b): Simulated versus measured vertical beam oscillation amplitudes at the location of BPM 17. The horizontal error bars of the measured amplitudes  $\epsilon_y^{\text{exp}}$  originate from the readout electronics of BPM 17 and the calibration factor  $\kappa$  (see Appendix B), whereas the vertical ones are determined by the circuit uncertainties using the PCE method, as described in Appendix C.

the systematic error of the readout electronics of BPM 17, nor will it affect the uncertainties of the elements of the driving circuit.

The fit shown in Fig. 13 yields  $\chi^2/\text{ndf} = 45.5/41$ , very close to unity (33). The linear fit yields a slope of  $0.999 \pm 0.018$ , which is perfectly consistent with unity. The intercept parameter of the fit yields  $(-0.93 \pm 0.31) \mu\text{m}$ , and within three standard deviations, it agrees with zero.

The very good agreement between measurements and simulations reflects our good understanding of both the electromagnetic fields generated in the WF and of the underlying beam dynamics in the machine. This point is further substantiated by comparing the simulated amplitudes at the WF and BPM positions with the estimated amplitudes expected from rescaling

based on the  $\beta$  functions<sup>9</sup>, taking into account the numerical values, listed in Table 1 of Appendix A,

$$\begin{aligned} \epsilon_y^{\text{WF}}|_{\text{sim}} &= (0.435 \pm 0.031) \mu\text{m}, \\ \sqrt{\frac{\beta_y^{\text{WF}}}{\beta_y^{\text{BPM}}}} \epsilon_y^{\text{BPM}}|_{\text{sim}} &= \epsilon_y^{\text{WF}}|_{\text{est}} = (0.435 \pm 0.039) \mu\text{m}. \end{aligned} \quad (25)$$

The good agreement between these two numerical values in Eq. (25) indicates that the observation of the oscillation amplitude at one location in the ring can be reliably transferred to some other place in the ring by use of Eq. (3). The above quoted value of  $\epsilon_y^{\text{WF}}|_{\text{sim}} = 0.435 \mu\text{m}$  is about a factor of 10 larger than the quantum limit of the vertical oscillation amplitude  $Q$ , given in Eq. (10).

In searches for EDMs in dedicated all-electric storage rings, a continuous monitoring of the orbits of the two counter-rotating beams is mandatory during data acquisition within the horizontal spin-coherence time (3). When intrabeam scattering can be neglected (24), which is arguably justified within the horizontal spin-coherence time, the beam can be described as a rarefied gas of particles, *i.e.*, the zero-point oscillations of individual particles are uncorrelated. Therefore, the quantum limit of the centroid of a bunch containing  $N$  particles can be estimated via  $Q_{\text{bunch}} = Q/\sqrt{N}$ . For a bunch of  $N = 10^{10}$  stored particles, one obtains  $Q_{\text{bunch}} \simeq 0.4 \text{ pm}$ , indicating that the systematic uncertainty of the beam oscillations will be rather limited by the sensitivity of the BPMs.

Finally, a satisfactory agreement has been achieved between Hooke's constant, simulated using the electromagnetic fields in the WF and the  $\beta$  functions of the COSY lattice, and the theoretical approximation of the no-lattice model assuming constant  $\beta$  functions of Eq. (8), yielding

$$\begin{aligned} k_{\text{H}}^{\text{sim}} &= (151.2 \pm 0.2) \text{ MeV/m}^2, \text{ and} \\ k_{\text{H}}^{\text{th}} &= 207 \text{ MeV/m}^2. \end{aligned} \quad (26)$$

---

<sup>9</sup>The uncertainty of the  $\beta$  functions amounts to about 10%, as discussed in Ref. (24).

The theoretical estimate of  $k_{\text{H}}^{\text{th}}$ , calculated using the numerical values listed in Table 1 of Appendix A, is about a factor of 1.4 larger than the simulated one. The given uncertainty of  $k_{\text{H}}^{\text{sim}}$  does not include the systematic scale uncertainty of the BPM calibration factor  $\kappa$  [see Eq. (29) in Appendix A]. At the matching point [see Eq. (20)], the Lorentz force amounts to

$$F_y^{\text{WF}} = k_{\text{H}}^{\text{sim}} \cdot \epsilon_y^{\text{WF}} \big|_{\text{sim}} \approx 66 \text{ eV/m} = 10.6 \text{ aN}, \quad (27)$$

where the intercept parameter has been ignored because of its smallness.

## 5 Conclusion and outlook

As part of several studies to investigate the performance of the waveguide RF Wien filter, exploratory data were taken to provide a benchmark on the sensitivity to very weak collective vertical beam oscillations of deuterons stored in the COSY ring. To a good approximation, the beam can be viewed as a rarefied gas of uncorrelated particles, and the sensitivity limit is applicable to the classical motion of individual particles, propagating along the ring circumference in the confining oscillatory potential. Simulations of the beam dynamics in the COSY ring equipped with an RF Wien filter suggest that with the present apparatus, the sensitivity to collective beam oscillations on the sub-micron level is within a factor of 10 of the amplitude of zero-point quantum oscillations of the stored deuterons. From the perspective of future EDM experiments, our finding confirms that the separation of the centroids of two counter-propagating beams may be determined to sub-picometer accuracy – the limitation is given by the sensitivity of the presently employed BPMs.

The reported excellent agreement between simulated and experimentally observed vertical beam oscillations at COSY suggests that a further increase in sensitivity to collective beam oscillations is possible. Specifically, the simulation on finer capacitor grids indicates that by further optimization of the WF settings to  $C_{\text{L}} = (692.76 \pm 1.00) \text{ pF}$  and  $C_{\text{T}} = (495.77 \pm 1.00) \text{ pF}$ ,

an oscillation amplitude at the WF location of  $\epsilon_y = (0.077 \pm 0.032) \mu\text{m}$  may be achieved. Thus in that case, the vertical oscillation amplitude would only be about a factor of 2 away from the quantum limit, with a corresponding Lorentz force of  $F_y \sim 3 \text{ aN}$ .

## Acknowledgments

This work has been performed in the framework of the JEDI collaboration and is supported by an ERC Advanced Grant of the European Union (proposal number 694340). In addition, it was supported by the Russian Fund for Basic Research (Grant No. 18-02-40092 MEGA) and by the Shota Rustaveli National Science Foundation of the Republic of Georgia (SRNSFG Grant No. DI-18-298: *High precision polarimetry for charged-particle EDM searches in storage rings*).

## A Quantities used in the beam simulations

In order to provide a consistent calculation of all effects in the storage ring, the beam simulations were carried out using the set of quantities given in Table 1 as an input. The vertical machine tune  $\nu_y$  is a result of simulations with the known COSY lattice, reflecting the actual currents of the magnetic elements in the machine at the time when the experiment was conducted. The simulations provide the uncalibrated parameters of the vertical beam oscillations to about per mill accuracy, and giving the kinematic, ring, and WF parameters to four digits appears therefore sufficient. It should be noted that within the simulation calculations carried out in the context of the present work, all quantities have been computed to double precision (machine epsilon of  $1.11 \cdot 10^{-16}$ ). Of the physical quantities, the highest sensitivity to the vertical betatron tune is exhibited by the theoretical estimate for Hooke's constant,  $dk_{\text{H}}^{\text{th}}/d\nu_y \approx 2 \cdot 10^3 \text{ MeV/m}^2$ . The largest uncertainty contributing to the error of the detected oscillation amplitudes arises from the BPM calibration factor  $\kappa$ , given in Eq. (29). It amounts to about 7.3% and is considered a systematic scale-factor uncertainty (see Appendix B).

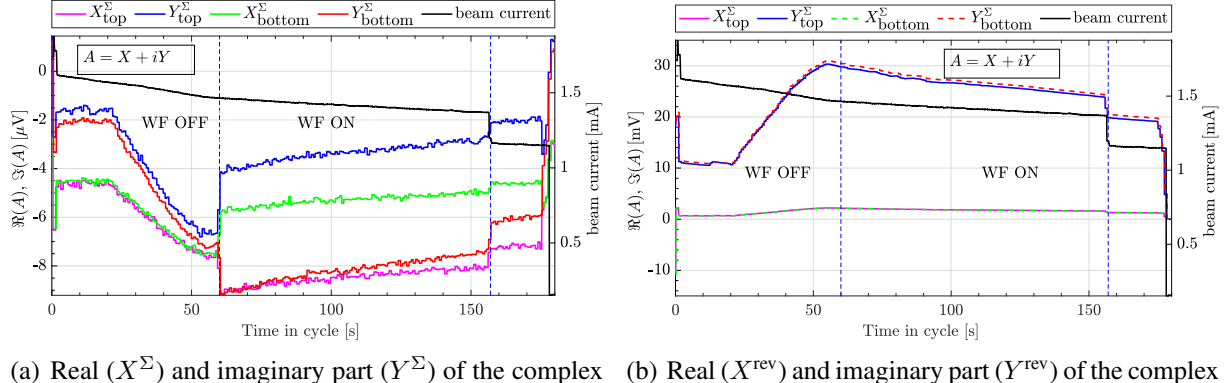
Table 1: Numerical values used for the beam simulations. The genuinely independent input parameters are listed in bold face. The derived quantities are displayed in normal font and are truncated to four decimal places.

Quantity	Symbol	Value
deuteron beam momentum	$\mathbf{p}$	970.0000 MeV/c
deuteron mass	$\mathbf{m}$	1875.6128 MeV/c <sup>2</sup>
deuteron $G$ factor	$\mathbf{G}$	-0.1430
Lorentz factor	$\beta$	0.4594
Lorentz factor	$\gamma$	1.1258
COSY circumference	$\mathbf{L}_{\text{COSY}}$	183.4728 m
revolution frequency	$f_{\text{rev}}$	750 603.7600 Hz
vertical machine tune	$\nu_y$	3.6040
vertical $\beta$ function at BPM 17	$\beta_y^{\text{BPM}}$	15.3049 m
vertical $\beta$ function at WF	$\beta_y^{\text{WF}}$	2.6784 m
effective length WF	$\ell$	1.1600 m
frequency WF	$f_{\text{WF}}$	871 000.0000 Hz
tune WF	$\nu_{\text{WF}} = \frac{f_{\text{WF}}}{f_{\text{rev}}}$	1.1604

## B Calibration of the BPM

The complex amplitudes measured by the lock-in amplifiers describe the magnitude and phase of each signal, and are here expressed by the corresponding real and imaginary components, denoted by  $X$  and  $Y$ , respectively, *i.e.*,  $A = X + iY$ . Examples of the data recorded at the sum frequency  $f^\Sigma$  and at the revolution frequency  $f^{\text{rev}}$  are shown in Fig. 14. The effect of switching on the power amplifiers of the WF at  $t = 60$  s is clearly visible. In both panels, one observes a separation of the quantities recorded by the top and bottom electrodes in the  $\mu\text{V}$  range for both frequencies after the WF is switched on. This separation is much more pronounced at the WF frequency than at the revolution frequency.

The quantities  $A_t^{\text{rev}}$  and  $A_b^{\text{rev}}$ , given in Eqs. (17), are related to a vertical beam offset  $\Delta y$  in



(a) Real ( $X^\Sigma$ ) and imaginary part ( $Y^\Sigma$ ) of the complex Fourier amplitudes  $A^\Sigma$  at the WF frequency. (b) Real ( $X^{\text{rev}}$ ) and imaginary part ( $Y^{\text{rev}}$ ) of the complex Fourier amplitudes  $A^{\text{rev}}$  at the revolution frequency.

Figure 14: Fourier amplitudes  $A = X + iY$  for the top and bottom electrodes of BPM 17 recorded by the lock-in amplifier as a function of time in the cycle at a strongly mismatched point ( $C_L = 907.79 \text{ pF}$  and  $C_T = 885.58 \text{ pF}$ ), at the WF frequency (a), and at the revolution frequency (b). In both panels, the stored beam current is shown in black. The cycle starts right after injection is completed at  $t = 0 \text{ s}$ , beam preparation continues until  $t = 55 \text{ s}$ , and the WF is switched on and data acquisition starts at  $t = 60 \text{ s}$ . At  $t = 156 \text{ s}$  the WF is switched off and data acquisition stops.

Table 2: Current variation  $\Delta I$  (in % of the maximum admissible current) in the vertical steerers to generate bumps and the corresponding position change of the vertical orbit  $\Delta y$  at the location of BPM 17.

$\Delta I$ (steerer) [%]	$\Delta y$ [mm]
-5	$-7.756 \pm 0.030$
-4	$-6.684 \pm 0.038$
-3	$-5.629 \pm 0.016$
-2	$-4.518 \pm 0.020$
-1	$-3.489 \pm 0.018$
0	$-2.439 \pm 0.029$
+1	$-1.429 \pm 0.020$
+2	$-0.288 \pm 0.028$
+3	$+0.798 \pm 0.044$
+4	$+1.872 \pm 0.014$
+5	$+2.928 \pm 0.069$

the following way,

$$R = \frac{A_t^{\text{rev}} - A_b^{\text{rev}}}{A_t^{\text{rev}} + A_b^{\text{rev}}} = \kappa \frac{2U_0 \Delta y}{2U_0} = \kappa \Delta y. \quad (28)$$

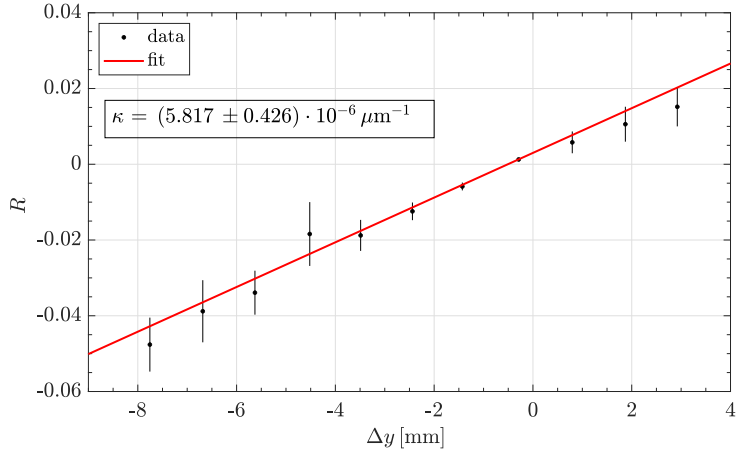


Figure 15: Calibration curve of BPM 17. The ratio  $R$ , defined in Eq.(28), depends on the introduced vertical beam offset  $\Delta y$  at the BPM.

The calibration constant  $\kappa$  is experimentally determined by introducing local *vertical* beam bumps in the ring at the location of BPM 17. These displacements  $\Delta y$  are invoked by altering the current of a set of vertical steerers, listed in Table 2. The calibration factor  $\kappa$  is obtained by fitting. Figure 15 shows the ratio  $R$  as a function of the vertical orbit variation  $\Delta y$ , exhibiting a nearly linear relation. The slope corresponds to

$$\kappa = (5.82 \pm 0.43) \cdot 10^{-6} \mu\text{m}^{-1}. \quad (29)$$

## C Uncertainty of the simulations

The uncertainties of the simulated amplitudes of the beam oscillations are computed using the Polynomial Chaos Expansion (PCE) algorithm. The functionality of the algorithm is explained below for one of the simulated data points of the map shown in Fig. 9.

The PCE algorithm offers an alternative to the well-known Monte-Carlo (MC) method without compromising the intended accuracy. It uses orthogonal polynomials to represent randomly changing variables to describe observables by means of a finite (truncated) series [for more details, see, e.g., Ref. (9)]. When the defined criteria of convergence are met, the expansion

---

**Algorithm 1:** Sparse Polynomial Chaos Expansion algorithm

---

**Data:** Generates Gaussian-distributed ensemble of uncertain circuit parameters using the Latin Hypercube Sampling (LHS) scheme  $X_i$

**Result:** Compute uncertainty of  $\epsilon_y$

Standardize input data  $X_i \rightarrow \xi_i$ ;

Guess hyperbolic truncation norm,  $q$ -norm;

Start with lowest possible expansion order  $p$ ;

Generate basis functions  $H_p(\xi_i)$  ( $p^{\text{th}}$  order Hermite polynomials);

Generate hyperbolically truncated set of basis functions  $H_p^q(\xi_i)$ ;

Apply Least-Angle Regression (LAR) algorithm;

Estimate optimum sparse set of basis functions  $H_p^{q*}(\xi_i)$ ;

Compute expansion coefficients  $C_j$  given  $\Gamma = \sum C_j H_p^{q*}(\xi_i)$ ;

Compute estimated values of  $\hat{\epsilon}_y = \Gamma \cdot \epsilon_y$ ;

Compute leave-one-out error  $\text{LOO}_{\text{err}}$ ;

Check convergence condition ( $\text{LOO}_{\text{err}} < 10^{-2}$ );

**while** *not convergent* **do**

- Enhance model (vary  $p$  and  $q$ );
- if** *convergent* **then**
  - Generate large sample of  $\hat{\epsilon}_y$ ;
  - Estimate statistical parameters;
  - Terminate algorithm;
- else**
  - Enrich input samples  $X_i$ ;
  - Repeat algorithm;

---

coefficients can be used to generate an arbitrarily large sample of observables, from which the uncertainties can be computed to the desired statistical accuracy.

The PCE algorithm has been compared with the MC method in many applications and has been shown to provide very reliable results. (30). The PCE requires much fewer simulations to converge compared to the MC method. For instance, for the present case, 200 beam tracking simulations per point in the 2D the map of beam oscillations, shown in Fig. 9 were sufficient to reach convergence.

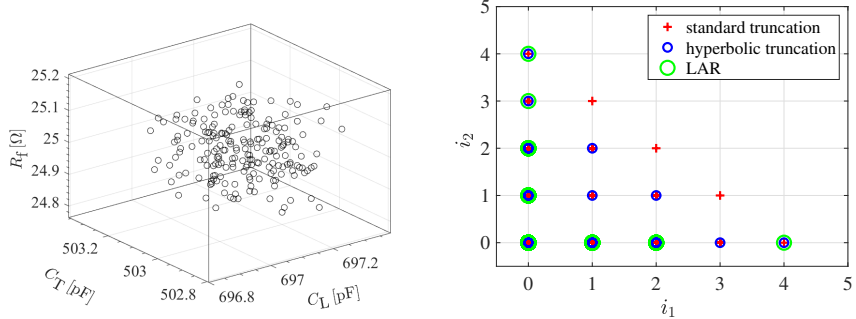
In cases where the number of random input variables  $m$  is larger than 10, the PCE method offers clear advantages over the MC method. The reason is that the number of basis functions in

the PCE method increases enormously as a consequence of the tensor product of the involved polynomials. Therefore, the algorithm has been improved further to allow for a reduction of the number of simulations required. Such an approach is also adopted here, as described in Algorithm 1. The hyperbolic truncation scheme together with the Least-Angle Regression (LAR) method form a sparse version of the original algorithm.

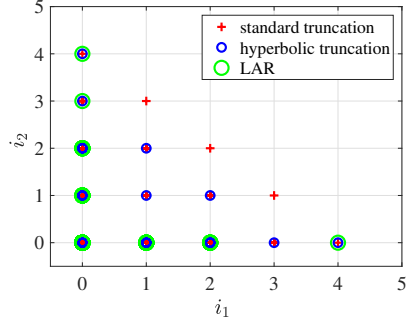
An  $m$ -dimensional set is first created, representing  $N$  combinations of simultaneous random variables. Many methods can be used to generate such sets, and here the Latin-hypercube sample scheme is adopted (16). Subsequently, the set is standardized for convergence reasons. Depending on the distribution of the data, the basis functions, here Hermite polynomials, are determined. The number of basis functions restricts the lower limit of the number of simulations (full-wave and tracking) which are usually computationally expensive. As a rule of thumb, with  $N$  basis functions, the PCE algorithm requires at least  $1.5 \times N$  (in this case, full-wave) simulations to converge. The number of basis functions itself can, however, be reduced by the hyperbolic truncation scheme that eliminates higher-order terms that do not have a significant impact on the observation objects (34, 35). Furthermore, by applying the LAR algorithm, the number of remaining basis functions can be further reduced substantially, whereby the problem becomes computationally solvable in a very efficient fashion.

The matching point, specified in Eq. (20), yields the minimum measurable beam oscillations, as given by Eq. (21). This experimental result can be estimated using the beam-tracking calculations. Subsequently, the concrete steps of the application of the PCE algorithm are discussed.

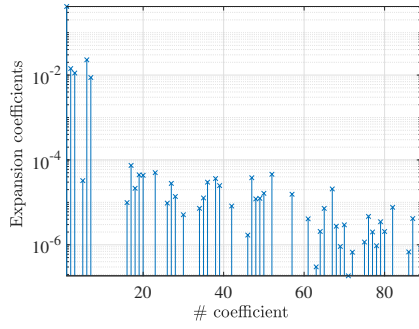
All the reasonable sources of uncertainties of the circuit are represented by 15 random parameters that are allowed to vary simultaneously. At first, a sample of  $(200 \times 15)$  entries is generated using the Latin-hypercube sampling scheme. As an example of this sample, the variation of the three circuit elements  $C_L$ ,  $C_T$ , and the load resistor  $R_f$  is shown in Fig. 16(a).



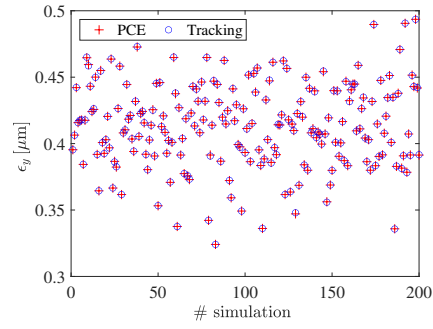
(a) Sample of  $C_L$ ,  $C_T$ , and  $R_f$  used in the PCE calculations showing a subset of the 15-dimensional input of random circuit uncertainties.



(b) Truncation schemes of the PCE algorithm.



(c) Expansion coefficients on a semi-log scale. 91 coefficients have been selected after applying the LAR algorithm to the matching point.



(d) Comparison between the tracking results and the PCE with respect to the oscillation amplitude, determined using the expansion coefficients of (c).

Figure 16: Intermediate results of the PCE algorithm applied at the matching point [see Eq. (20)]. Quantitative results of the PCE algorithm are summarized in Table 3.

All the uncertain parameters in the electromagnetic circuit simulations are used to generate the electric and magnetic fields shown in Fig. 10. These are subsequently used in the beam-tracking calculations. For the matching point of the map [Eq. (20)],  $N = 200$  full-wave simulations were conducted. The import of these field maps into the beam-tracking calculations resulted in a set of  $N = 200$  values of  $\epsilon_y$ . This set is not directly used to conduct the statistical analysis. Instead, in conjunction with the input samples, these data are used as input to the sparse PCE algorithm.

Table 3: PCE simulation parameters of the matching point in Eq. (20).

parameter	value
order of expansion $p$	6
dimension $m$	15
hyperbolic truncation $q$	0.35
leave-one-out error $\text{LOO}_{\text{err}}$	$1.71 \cdot 10^{-4}$
number of used basis functions $P^{\text{LAR}}$	91
number of used full-wave simulations $N$	200

The optimum set of basis function is determined using the LAR algorithm, as shown in Fig. 16(b). With an expansion order of  $p = 6$  and a truncation norm  $q = 0.35$ , executing the PCE algorithm required 91 basis functions to converge, reflected by the low value of the leave-one-out error  $\text{LOO}_{\text{err}} = 1.7 \cdot 10^{-4}$ . Subsequently, the expansion coefficients are computed, qualitatively depicted in Fig. 16(c). It is shown in Fig. 16(d) that the PCE algorithm perfectly reproduces the tracking results using these expansion coefficients. Finally, these coefficients are used to reconstruct a larger sample of  $\epsilon_y$  to estimate the error  $\sigma_{\epsilon_y}$ . Figure 11 shows  $10^6$  reconstructed samples. The PCE parameters used are summarized in Table 3.

The fitting of these results with a Gaussian, as depicted in panel (b) of Fig. 11, yields a standard deviation of  $\sigma_{\epsilon_y} = 0.082 \mu\text{m}$ . The same technique is repeated for each point in the map.

## References

1. M. Pospelov and A. Ritz, “Electric dipole moments as probes of new physics,” *Annals of Physics*, vol. 318, no. 1, pp. 119 – 169, 2005. Special Issue.
2. W. Bernreuther, “CP violation and baryogenesis,” *Lect. Notes Phys.*, vol. 591, pp. 237–293, 2002, hep-ph/0205279.

3. F. Abusaif *et al.*, “Storage Ring to Search for Electric Dipole Moments of Charged Particles - Feasibility Study,” 12 2019, 1912.07881.
4. R. Maier, “Cooler synchrotron {COSY} — performance and perspectives,” *Nuclear Instruments and Methods in Physics Research Section A: Accelerators, Spectrometers, Detectors and Associated Equipment*, vol. 390, no. 1–2, pp. 1 – 8, 1997.
5. F. Rathmann, A. Saleev, and N. N. Nikolaev, “The search for electric dipole moments of light ions in storage rings,” *J. Phys. Conf. Ser.*, vol. 447, p. 012011, 2013.
6. W. M. Morse, Y. F. Orlov, and Y. K. Semertzidis, “rf Wien filter in an electric dipole moment storage ring: The “partially frozen spin” effect,” *Phys. Rev. ST Accel. Beams*, vol. 16, no. 11, p. 114001, 2013.
7. F. Rathmann, N. N. Nikolaev, and J. Slim, “Spin dynamics investigations for the electric dipole moment experiment,” *Phys. Rev. Accel. Beams*, vol. 23, p. 024601, Feb 2020.
8. J. Slim, R. Gebel, D. Heberling, F. Hinder, D. Hölscher, A. Lehrach, B. Lorentz, S. Mey, A. Nass, F. Rathmann, L. Reifferscheidt, H. Soltner, H. Straatmann, F. Trinkel, and J. Wolters, “Electromagnetic Simulation and Design of a Novel Waveguide {RF} Wien Filter for Electric Dipole Moment Measurements of Protons and Deuterons,” *Nuclear Instruments and Methods in Physics Research Section A: Accelerators, Spectrometers, Detectors and Associated Equipment*, vol. 828, pp. 116 – 124, 2016.
9. J. Slim, F. Rathmann, A. Nass, H. Soltner, R. Gebel, J. Pretz, and D. Heberling, “Polynomial chaos expansion method as a tool to evaluate and quantify field homogeneities of a novel waveguide rf wien filter,” *Nuclear Instruments and Methods in Physics Research Section A: Accelerators, Spectrometers, Detectors and Associated Equipment*, vol. 859, no. Supplement C, pp. 52 – 62, 2017.

10. J. Slim, *A novel waveguide RF Wien filter for electric dipole moment measurements of deuterons and protons at the COoler SYnchrotron (COSY)/Jülich*. Dissertation, Rheinisch-Westfälische Technische Hochschule Aachen, Aachen, 2018. Published on the publication server of RWTH Aachen University. Awarded the Borchers Plakette and the Friedrich Wilhelm Prize 2019. Dissertation, Rheinisch-Westfälische Technische Hochschule Aachen, 2018, <https://publications.rwth-aachen.de/record/748558>.
11. S. Schreppler, N. Spethmann, N. Brahms, T. Botter, M. Barrios, and D. M. Stamper-Kurn, “Optically measuring force near the standard quantum limit,” *Science*, vol. 344, no. 6191, pp. 1486–1489, 2014, <https://science.sciencemag.org/content/344/6191/1486.full.pdf>.
12. B. Abbott *et al.*, “Observation of a kilogram-scale oscillator near its quantum ground state,” *New J. Phys.*, vol. 11, p. 073032, 2009.
13. K. W. Murch, K. L. Moore, S. Gupta, and D. M. Stamper-Kurn, “Observation of quantum-measurement backaction with an ultracold atomic gas,” *Nature Physics*, vol. 4, pp. 561–564, Jul 2008.
14. M. J. Biercuk, H. Uys, J. W. Britton, A. P. VanDevender, and J. J. Bollinger, “Ultrasensitive detection of force and displacement using trapped ions,” *Nature Nanotechnology*, vol. 5, pp. 646–650, Sep 2010.
15. D. Rugar, R. Budakian, H. J. Mamin, and B. W. Chui, “Single spin detection by magnetic resonance force microscopy,” *Nature*, vol. 430, pp. 329–332, Jul 2004.
16. J. Slim, A. Nass, F. Rathmann, H. Soltner, G. Tagliente, and D. Heberling, “The driving circuit of the waveguide RF wien filter for the deuteron EDM precursor experiment at COSY,” *Journal of Instrumentation*, vol. 15, pp. P03021–P03021, mar 2020.

17. S. Martin, D. Prasuhn, W. Schott, and C. Wiedner, “A storage ring for the julic cyclotron,” *Nuclear Instruments and Methods in Physics Research Section A: Accelerators, Spectrometers, Detectors and Associated Equipment*, vol. 236, no. 2, pp. 249 – 255, 1985.
18. P. Forck, P. Kowina, and D. Liakin, “Beam position monitors,” in *CAS - CERN Accelerator School: Course on Beam Diagnostics* (D. Brandt, ed.), CERN Accelerator School, p. 188, CERN, 2008.
19. J. Dietrich, V. Kamerdzhev, V. Parkhomchuk, V. Reva, and M. Bryzgunov, “2 MeV Electron Cooler at COSY Juelich,” *ICFA Beam Dyn. Newslett.*, vol. 64, pp. 75–86, 2014.
20. H.-H. Adam *et al.*, “Proposal for the wide angle shower apparatus (WASA) at COSY-Julich: WASA at COSY,” 10 2004, nucl-ex/0411038.
21. F. Müller, *Polarimeter Development for Electric Dipole Moment Measurements in Storage Rings*. PhD thesis, RWTH Aachen University, 2019.
22. F. Müller, O. Javakhishvili, D. Shergelashvili, I. Keshelashvili, D. Mchedlishvili, F. Abu-saif, A. Aggarwal, L. Barion, S. Basile, J. Böker, N. Canale, G. Ciullo, S. Dymov, O. Felden, M. Gagoshidze, R. Gebel, N. Demary, K. Grigoryev, D. Grzonka, T. Hahnrahs, V. Hejny, A. Kacharava, V. Kamerdzhev, S. Karanth, A. Kulikov, A. Lehrach, P. Lenisa, N. Lomidze, B. Lorentz, G. Macharashvili, A. Magiera, Z. Metreveli, A. Nass, N. Nikolaev, M. Nioradze, A. Pesce, V. Poncza, D. Prasuhn, J. Pretz, F. Rathmann, A. Saleev, T. Sef-zick, Y. Senichev, V. Shmakova, J. Slim, H. Soltner, E. Stephenson, H. Ströher, M. Tabidze, G. Tagliente, Y. Uzikov, Y. Valdau, T. Wagner, A. Wrońska, P. Wüstner, and M. Żurek, “A new beam polarimeter at COSY to search for electric dipole moments of charged particles,” *Journal of Instrumentation*, vol. 15, pp. P12005–P12005, dec 2020.

23. A. Lehrach and R. Maier, “Siberian Snake for the Cooler Synchrotron COSY,” *Conf. Proc. C*, vol. 0106181, pp. 2566–2568, 2001.
24. C. Weidemann *et al.*, “Toward polarized antiprotons: Machine development for spin-filtering experiments,” *Phys. Rev. ST Accel. Beams*, vol. 18, no. 2, p. 020101, 2015, 1407.6724.
25. M. Meade, *Lock-in Amplifiers: Principles and Applications*. IEE electrical measurement series, P. Peregrinus, 1983.
26. H. Huang *et al.*, “Overcoming an intrinsic depolarizing resonance with a partial Siberian snake,” *Phys. Rev. ST Accel. Beams*, vol. 7, p. 071001, 2004.
27. R. Aster, B. Borchers, and C. Thurber, *Parameter Estimation and Inverse Problems*. Elsevier Science, 2018.
28. A. Wolski, *Beam Dynamics in High Energy Particle Accelerators*. IMPERIAL COLLEGE PRESS, 2014, <https://www.worldscientific.com/doi/pdf/10.1142/p899>.
29. D. Sagan, “Bmad: A relativistic charged particle simulation library,” *Nucl. Instrum. Meth.*, vol. A558, no. 1, pp. 356–359, 2006. Proceedings of the 8th International Computational Accelerator Physics Conference.
30. R. C. Smith, *Uncertainty Quantification: Theory, Implementation, and Applications*. USA: Society for Industrial and Applied Mathematics, 2013.
31. P. Offermann, H. Mac, T. T. Nguyen, S. Clénet, H. D. Gersem, and K. Hameyer, “Uncertainty quantification and sensitivity analysis in electrical machines with stochastically varying machine parameters,” *IEEE Transactions on Magnetics*, vol. 51, pp. 1–4, March 2015.

32. A. Adelmann, “On uncertainty quantification in particle accelerators modelling,” 2018, 1509.08130.
33. D. York, N. M. Evensen, M. López Martínez, and J. De Basabe Delgado, “Unified equations for the slope, intercept, and standard errors of the best straight line,” *American Journal of Physics*, vol. 72, no. 3, pp. 367–375, 2004, <https://doi.org/10.1119/1.1632486>.
34. B. Sudret and A. Der Kiureghian, *Stochastic finite element methods and reliability: a state-of-the-art report*. Department of Civil and Environmental Engineering, University of California, 2000.
35. B. Sudret, “Global sensitivity analysis using polynomial chaos expansions,” *Reliability Engineering & System Safety*, vol. 93, no. 7, pp. 964–979, 2008.